Initial results of combining GPS occultations with ECMWF global analyses within a 1DVar framework

E. Robert Kursinski[1*], Sean B. Healy[2], and Larry J. Romans[1]

[1]*MS 238-600 Jet Propulsion Laboratory, California Institute of Technology, Pasadena, CA 91109-8099, U.S.A.*
[2]*Numerical Weather Prediction Division (Room 338), The Met Office, London Road, Bracknell RG12 2SZ, U.K.*

We present results of combining occultation refractivity profiles from GPS/MET with ECMWF global analyses in a 1DVar framework in order to separate the wet and dry contributions to refractivity and assess their impact on the analyzed temperature, surface pressure and specific humidity fields. We find significant zonal mean temperature, surface pressure and humidity differences between the 1DVar solutions and the ECMWF analyses reflecting biases between the GPS refractivities and ECMWF analyses. Large profile-to-profile temperature discrepancies in the tropical lower stratosphere are due to waves not represented in the analyses. The 1DVar solution is generally drier than ECMWF particularly in the southern subtropics. Lack of moisture above 300 hPa in the present model caused the solution to make large adjustments in low latitude surface pressure and tropospheric temperatures to increase upper troposphere densities and compensate for the missing upper level moisture. The discrepancies between the solution and the background and observational data sets represent roughly a 2-sigma level of agreement rather than the 1-sigma level desired in a 1DVar solution. Given the simplicity of our error covariances, our results are promising as a first step. In the future, the error covariances need to be refined and, in particular, to vary with location.

1. Introduction

We describe a set of initial results of combining GPS occultation refractivity profiles with a set of ECMWF global weather analyses in a 1D variational (1DVar) assimilation scheme. The occultations, which number approximately 800, were acquired by GPS/MET from June 21 to July 4, 1995. One goal here is to derive temperature and moisture profiles from the GPS results using the ECMWF analyses as background information to provide the constraints needed to separate the wet and dry contributions to the refractivity which GPS measures. Alternatively one can view the purpose of this effort as using GPS observations to improve weather analyses. Ultimately this work represents a step toward combining the unique features of the GPS observations with other observations and modeling to improve weather forecasting and analyses and our understanding of the behavior of our climate system.

2. GPS Occultation Background

The GPS to low-Earth-orbiter (LEO) occultation geometry is shown in Fig. 1. Relative motion between the transmitter and receiver produce a limb scan of the atmosphere in roughly 60 seconds. From measurements of Doppler shift and knowledge of the viewing geometry, the bending angle, α, and asymptotic miss distance, a, are derived. The index of refraction, n, as a function of radius from the center of

curvature, r, is derived from $\alpha(a)$ via an Abelian integral transform relation under the assumption of local spherical symmetry (Fjeldbo *et al.*, 1971). At microwave wavelengths refractivity (defined as $N = [n-1]10^6$) is given as

$$N = b_1\frac{P}{T} + b_2\frac{P_w}{T^2} \qquad (1)$$

where P is pressure, P_w is partial pressure of water vapor, T is temperature and b_1 and b_2 are constants equal to 77.6 K hPa^{-1} and 3.73×10^5 K^2 hPa^{-1} respectively. Because of its permanent dipole moment, each water vapor molecule contributes approximately 15 to 20 times the refractivity of an average dry (N_2 or O_2) molecule and water therefore contributes significantly to refractivity in the lower troposphere. In the cold, dry conditions of the upper troposphere and above ($T < 230$ K) water contributes little to refractivity and profiles of refractivity are directly proportional to density. Hydrostatically integrating density yields a profile of pressure (or equivalently geopotential), and knowing density and pressure yields temperature. Given additional temperature information, water vapor can be derived in the middle and lower troposphere.

Coverage and Resolution: A single orbiting GPS receiver with fore and aft antennas can observe between 500 and 700 daily occultations distributed globally, a number which can be roughly doubled by adding a GLONASS receive capability. NASA's GPS Earth Observatory (GEO) will consist of several orbiting GPS occultation receivers by the end of 2000 including, CHAMP, SAC-C and IOX which will produce more than 1000 occultations per day rivaling the present global radiosonde network but with far more even distribution of coverage. The limb-viewing geometry of the

*Now at Department of Atmospheric Science, University of Arizona, P.O. Box 210081, Tucson, AZ 85721-0081, U.S.A.
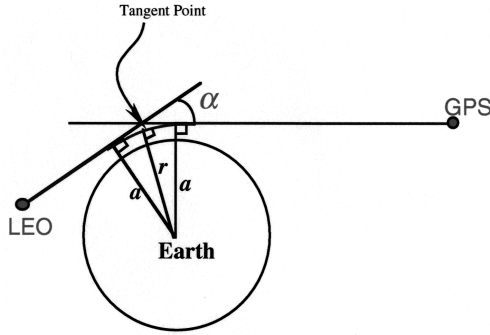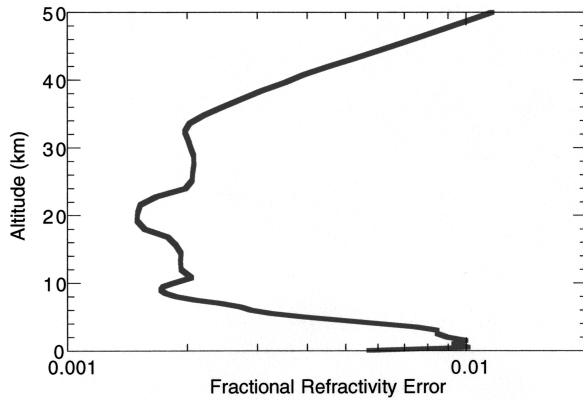
Fig. 1. Occultation geometry.

Fig. 2. Square root of diagonal terms of the measurement fractional refractivity error covariances.

occultation observations creates a pencil-like sampling volume with along-track resolution of order 200–300 km vertical and cross-track resolution of order 1 km or better as defined by Fresnel diffraction. Sub-Fresnel resolution is achievable through reduction of diffraction effects (Karayel and Hinson, 1997).

Predicted Accuracy: Figure 2 shows the expected fractional refractivity errors versus height based on a detailed examination of refractivity, temperature and pressure errors by Kursinski *et al.* (1997). Fractional temperature and pressure errors are similar yielding sub-Kelvin temperature and ∼10 m geopotential height accuracies from the upper troposphere into the lower stratosphere. Horizontal gradients are the dominant refractivity error source near the surface and are primarily responsible for the increasing fractional error at lower altitudes. GPS/MET temperatures are consistent with the ECMWF analyses at the 1 to 1.5 K level (Kursinski *et al.*, 1996; Rocken *et al.*, 1997) while geopotential comparisons with ECMWF are consistent at the 20 m level (Leroy, 1997). Kursinski *et al.* (1995) and Kursinski and Hajj (2000a) estimated the RMS accuracy of water vapor profiles derived from GPS refractivity profiles to be 0.2 g/kg in drier regions increasing to 0.5 g/kg in wetter regions with of the order of 0.1 g/kg depending on the accuracy of assumed temperature.

3.   1DVar Retrieval Overview

Here we briefly summarize the 1D variational approach used in this study. For further details see Healy and Eyre (2000). In a variational retrieval, the most probable atmospheric state, x, is calculated by combining *a priori* (or background) atmospheric information, x^b, with the measurements/observations, y^o, in a statistically optimal way. The solution, x, gives the best fit—in a least squared sense—to both the observations and *a priori* information. It can be shown in the case of Gaussian error distributions, that obtaining the most probable state is equivalent to minimizing a cost function $J(x)$ given by,

$$J(x) = \frac{1}{2}(x - x^b)^T B^{-1}(x - x^b)$$
$$+ \frac{1}{2}(y^o - H(x))^T (E + F)^{-1}(y^o - H(x)) \quad (2)$$

where B is the expected background error covariance matrix; $H(x)$ is the forward model, mapping the atmospheric information x into measurement space; E and F are the expected error covariances of measurements and forward model respectively. The superscripts T and -1 denote matrix transpose and inverse. Note that the normalized form has allowed us to combine "apples" (an atmospheric model state vector) and "oranges" (GPS observations of bending angles or refractivity). The error covariance of the solution, x, is

$$B' = [B^{-1} + K^T (E + F)^{-1} K]^{-1} \quad (3)$$

where K is $\nabla_x y^o$, the gradient of y^o with respect to x.

Implementation: In this analysis, the measurement vector, y^o, is a one dimensional vertical profile of refractivity as a function of geopotential height ($y^o_m = N(z_m)$), at a fixed tangent point location. With GPS occultations, y^o could consist of bending angles or refractivity. Although using refractivity derived via the Abel transform is not as accurate because of the spherical symmetry approximation, it is much simpler than use of bending angles which requires a more complicated forward operator. The background state vector, x^b, is a profile extracted from global analyses available every 6 hours from the European Centre for Medium-range Weather Forecasts (ECMWF), derived by interpolating the model fields to the locations of the occultation tangent points and extracting the vertical profile information. It contains 46 elements: 30 temperature values on fixed pressure levels ($T_i = T(P_i)$) between 1000–10 hPa, 15 ln (specific humidity (g/kg)) ($\ln Q_i = \ln Q(P_i)$) values on the lowest 15 levels (between 1000–300 hPa) and the surface pressure. Note that the ln Q values are zero at altitudes above the 300 hPa level, which turns out to have important consequences as we will discuss in Section 5. The background covariance matrix, B, is based on a subset of that used in the operational processing of TOVS data at UKMO (Gadd *et al.*, 1995) and includes a full covariance structure. The temperature and specific humidity errors from the diagonal terms of the background error covariance matrix are shown in Figs. 3 and 4 respectively. Relatively large temperature errors near 200 hPa reflect the uncertainties near the northern mid-latitude tropopause. The diagonal error term associated with the surface pressure is 2.5 hPa.
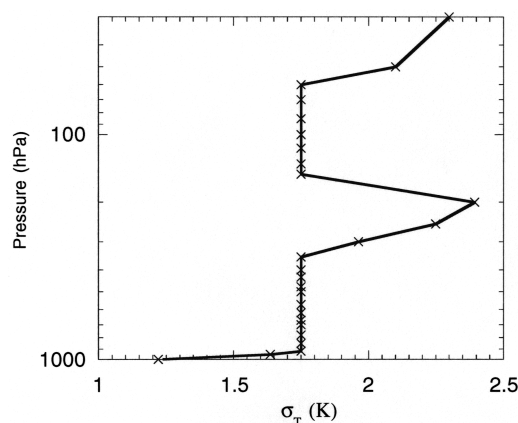
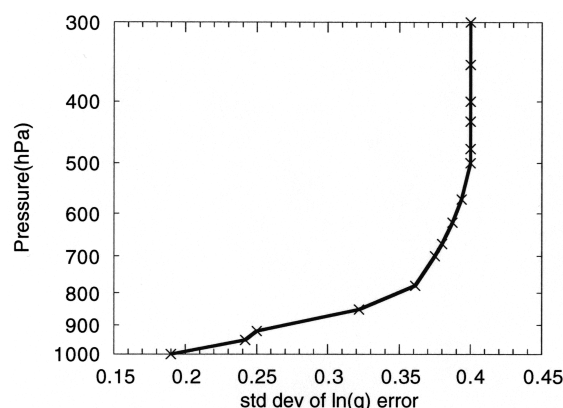Fig. 3. Square root of diagonal terms of temperature error covariances.

Fig. 4. Square root of diagonal terms of specific humidity error covariances.

The forward model: $H(x^n)$: The forward model 'H' evaluates a model refractivity value, N, for each 'observed' geopotential height, z_m, using the current state vector estimate, x^n. The derivation of the refractivity profile from state vector is composed of the following steps. Firstly, the virtual temperature on the fixed pressure levels is calculated. The hydrostatic equation is then integrated, assuming the virtual temperature varies linearly with geopotential height between the pressure levels which enables evaluation of the gradients of log (specific humidity), temperature and virtual temperature with respect to geopotential height. The specific humidity, temperature and pressure values can then be calculated at an observation geopotential height, z_m. This formulation of the model ensures that the refractivity, pressure, temperature and humidity are continuous over the vertical profile.

Observation Errors: The refractivity measurement error covariance matrix, E, is estimated from Fig. 2. The variance values, σ_m^2, are calculated assuming the percentage error in the refractivity is 1% at the surface and falls linearly with height to 0.2% at 10 km above which the percentage error is constant at this value to 35 km altitude ($\sim$10 hPa). Since the discrete form of the Abel transform is simply a weighted sum of the bending angle values, vertical correlations exist between the refractivity values such that the off-diagonal terms of E, E_{nm}, are non-zero even if the bending angle er-

rors are uncorrelated. In this work, these are approximated assuming an exponential decay with separation in geopotential height given by, $E_{nm} = \sigma_n \sigma_m \exp(-l(z_n - z_m))$ where l is the inverse of a scale length with a numerical value of chosen to be 3×10^{-4} m^{-1}. This model has been compared with covariances evaluated from the impulse response of an Abel transform routine with the assumption of uncorrelated bending angle errors, and it shows reasonable agreement.

Forward model errors: The forward model in this case is simply the refractivity equation (1) plus the interpolation from the model pressure levels to the observational geopotential height levels. The dry part of (1) is accurate to 0.02% and the wet part is accurate to $\sim$1% (Kursinski *et al.*, 1997). In comparison to other sources of error, these contributions are small and can therefore be ignored. The approach used to interpolate from model pressure levels to observed geopotential heights is very accurate and the interpolation errors will be small to the extent that the model levels are spaced sufficiently close to represent the atmospheric structure captured by the observations. Issues regarding model representativeness (how well can the model actually represent the behavior captured in the observations), and vertical resolution sufficient to capture the important aspects of the observations are discussed by Kursinski *et al.* (2000). For the purposes of the present study, since the errors in the forward model are small, we have set the F matrix to 0.

4. 1DVar Results Using GPS/MET Data

We have combined refractivity profiles derived from GPS/MET occultation observations from June 21 to July 4, 1995 with background state vectors from the nearest 6-hour ECMWF analysis, interpolated to the location of each occultation. The data period was chosen because the GPS Anti-Spoofing (AS) encryption was off and the software in the GPS/MET receiver during this period enabled the profiles to extend to within 1 km of the surface much of the time.

We discuss the 1DVar results in terms of temperature, surface pressure, and specific humidity differences between the background and solution and in terms of refractivity differences between the observations and solution. The differences are characterized by the mean and standard deviation of their zonal (latitude versus height) behavior.

4.1 1DVar temperature results

Near the surface, the small size of the mean solution minus background (S − B) temperature differences in Fig. 5 reflects the relatively small background temperature error at 1000 hPa (Fig. 3) and the limited number of occultations penetrating all the way to the surface. Above the surface, there are significant differences between the solution and background temperature due to the refractivity observations. The solution is significantly warmer than the background (S − B > 0) in the low-latitude, lower troposphere between 65S and 60N and in the low latitude, near-tropopause region as well as near 50 hPa near 20S and 30N. Much of the Northern Hemisphere north of 60N and the Southern Hemisphere south of 50S and above 400 hPa have cooled as have the uppermost regions near 30 hPa. The most extensive and largest temperature increases in the solution occur between 15S and 30N between 800 and 400 hPa with shifts of 2 to 4 K representing 1 to 2 sigma shifts in mean temperatures! Such shifts are surprising
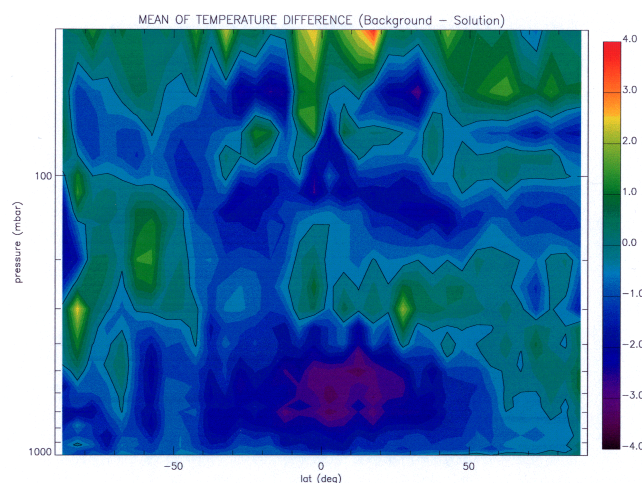
Fig. 5.   Latitude and height dependence of zonal mean of Background minus Solution temperatures in Kelvin. The black line indicates the zero difference contour.
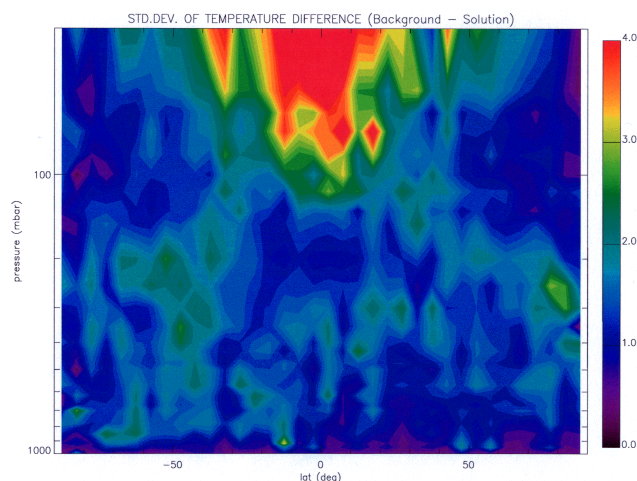

Fig. 7.   Latitude dependence of Background minus Solution surface pressure in hPa. Solid line is mean and dashed line is standard deviation.

Fig. 6.   Latitude and height dependence of zonal standard deviation of Background minus Solution temperatures in Kelvin.

because refractivity should more directly influence specific humidity rather than temperature in warm, wet regions. We believe these changes result indirectly from the lack of water vapor above the 300 hPa level in the model (see Section 5). The low latitude tropopause warming is also a bit surprising and deserves a more thorough examination because we would expect the higher vertical resolution of the GPS results to better capture the extremely cold temperatures at the tropopause than other satellite observations which are assimilated into the analyses. Meridional bands also evident in the mean adjustments in tropospheric and stratospheric temperatures imply the solution is adjusting the temperature lapse rate relative to the background and altering the atmospheric stability.

Near-surface temperatures do not show much change in terms of standard deviation of differences between solution and background temperatures (Fig. 6). Standard deviations in most of the region below the 100 hPa level are in the 1 to
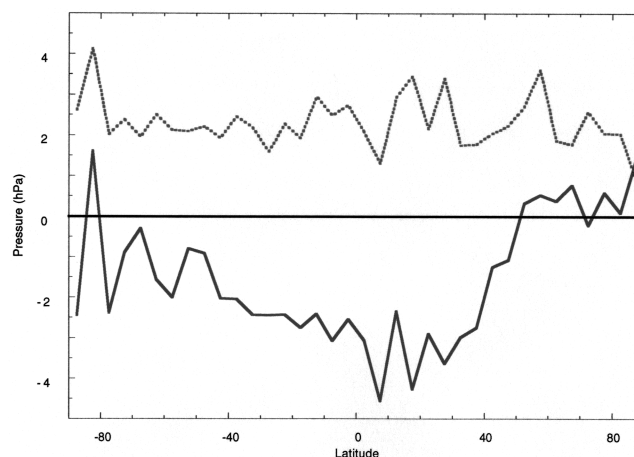
2.5 K range which is reasonable given that the background temperature errors are roughly 1.7 K (Fig. 3). Standard deviations in the Southern Hemisphere appear to be somewhat larger than their Northern Hemisphere counterparts in general. The region of largest standard deviations of more than 4 K in the tropical lower stratosphere reflect the large amount of wave activity in this zone which is apparent in the GPS occultations (Kursinski *et al.*, 1996; Kursinski, 1997; Tsuda *et al.*, 1999). The 1 to 3 km vertical wavelengths of these waves are resolved by the GPS occultations but not by operational satellite observations or the ECMWF global analyses. The large variations in Figs. 5 and 6 relative to the background errors in Fig. 3 indicate that the background temperature error covariances should vary with location.

4.2   1DVar surface pressure results

Figure 7 shows the mean and standard deviation of S − B surface pressure difference versus latitude. North of 50N, the solution has a slightly smaller average surface pressure of about 0.5 hPa than the background generally indicating good agreement where there are relatively many radiosonde observations. South of 45S, the solution surface pressure is larger than that of the background by 1 to 2 hPa. This may reflect a real bias between the analyses and reality but may also reflect the impact of sub-optimal background temperature, pressure and specific humidity error covariances at high southern latitudes. Between 40S and 40N, the solution surface pressure is 2 to 4 hPa higher than the background representing mean shifts in the solution of the order of 1 sigma (= 2.5 hPa). The large, mean, low latitude surface pressure adjustments likely result from the lack of model moisture above the 300 hPa level (see Section 5). The standard deviation of the surface pressure differences between background and solution are approximately 2 to 3 hPa which is consistent with the 1-sigma (2.5 hPa) background error estimate.

4.3   1DVar specific humidity results

Throughout much of the troposphere the solution's mean specific humidity is drier than the background by 20% or more (Fig. 8) similar to results of Kursinski and Hajj (2000a). Regions of large S − B standard deviations in Fig. 9 generally coincide with the large drying regions indicating significant
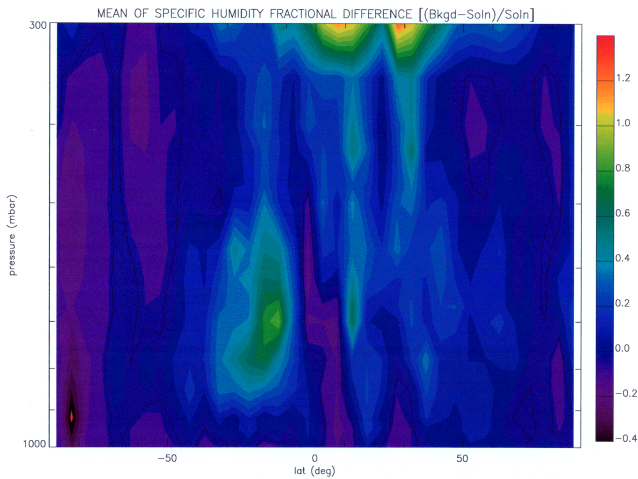
Fig. 8.   Latitude and height dependence of zonal mean of Background minus Solution specific humidity in (Background − Solution)/Solution. The black line indicates the zero difference contour.

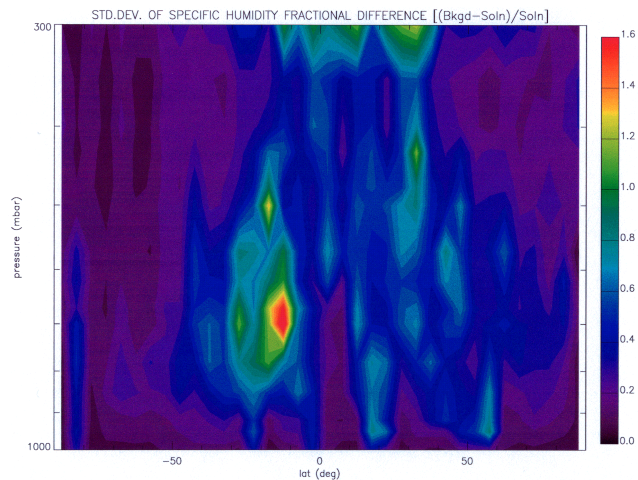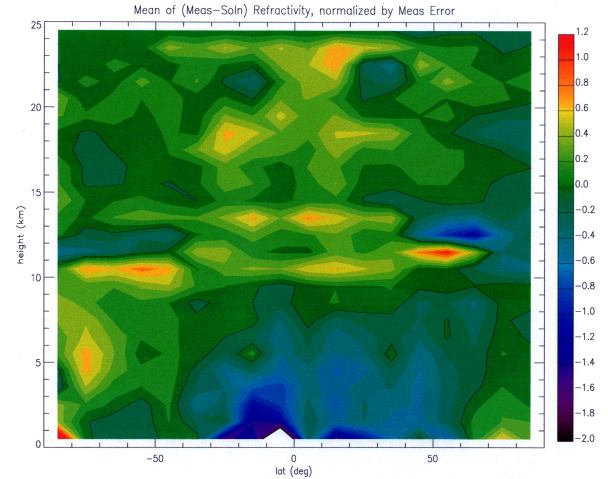Fig. 10.   Latitude and height dependence of zonal mean of Observation minus Solution refractivity normalized to the *a priori* observational refractivity errors defined in Fig. 2. The black line indicates the zero difference contour.

Fig. 9.   Latitude and height dependence of zonal standard deviation of Background minus Solution specific humidity in (Background − Solution)/Solution.
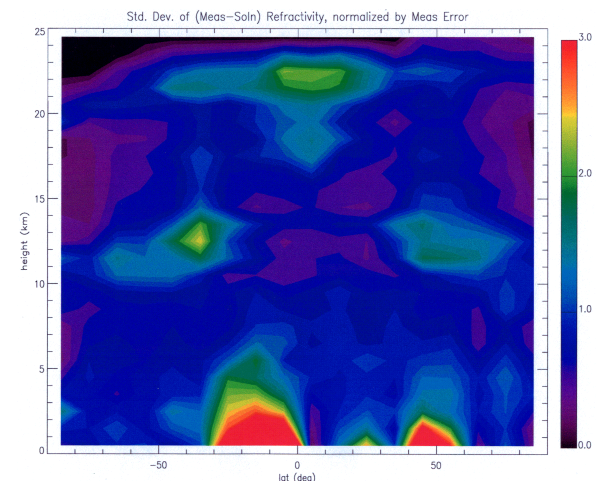

Fig. 11.   Latitude and height dependence of zonal standard deviation of Observation minus Solution refractivity normalized to the *a priori* observational refractivity errors defined in Fig. 2.

disagreement between model and observations in the individual profile structure as well as their average. Drying and standard deviations are very large in the southern subtropics between 5S and 30S and 900 and 500 hPa reaching a peak near 15S and 700 hPa consistent with the systematic rounding off of the very sharp PBL top in this area by the background analyses (Kursinski and Hajj, 2000a). Large discrepancies close to 300 hPa near the latitudes of the Inter-Tropical Convergence Zone (ITCZ) and Indian-Asian monsoons are likely related to the solution attempting to reconcile the sharp model cutoff in moisture above the 300 hPa level with the observations which have no such cutoff (Section 5). The 10–20% moistening of the solution at high southern latitudes is surprising given the low specific humidities there. The 20% moistening near the ITCZ below 500 hPa amid drying in the surrounding regions reflects closer agreement between the model and observed refractivities in this region and probably also reflects some influence from the lack of model moisture

above 300 hPa (Section 5).

4.4   Consistency of the measurement and solution refractivity structure

Figures 10 and 11 show the mean and standard deviation of the differences between the solution and observed refractivities versus height (not pressure) relative to the measurement error covariance. North of 40S and below 8 km, the solution refractivity is generally larger than observed and smaller than the background refractivity. This significant refractivity difference between the observations and ECMWF analyses has been interpreted by Kursinski and Hajj (2000a) as a moist bias in the ECMWF analyses in this region, particularly in the southern subtropics within a few kilometers of the surface. At higher altitudes and latitudes, there are sharp changes in color (red to blue) in Fig. 10 near 12 km in the Northern and 11 km in the Southern Hemispheres near regions of relatively high standard deviation in Fig. 11, that

may reflect unresolved tropopause structure in the ECMWF analyses. Above 9 km at low latitudes, the solution tends to have less refractivity (lower densities) than observed. In the tropical, lower stratosphere, measurement minus solution standard deviations are larger than 1 sigma likely indicating that the solution was unable to fully represent the waves observed in the occultations to within the 1 sigma refractivity errors in Fig. 2. This probably indicates the background temperature errors are too small and the vertical resolution in the ECMWF analyses is too coarse in this region.

5. Impact of No Model Water above 300 hPa

In the 1D model, water vapor extends from the surface to 300 hPa while specific humidities in the real world extend above the 300 hPa level. In the tropical and monsoonal zones, specific humidities at these levels can be 0.5 g/kg or more (Kursinski and Hajj, 2000a), and contribute more than 1% in refractivity. To compensate for the missing water vapor refractivity, the solution must increase the dry density above the 300 hPa level ($\sim$9.5 km altitude) by increasing the pressure at these heights and decreasing the temperature between 300 hPa and 200 hPa ($\sim$12 km altitude). To increase hydrostatic pressure at a given altitude, the solution increases temperatures at lower altitudes and increases the surface pressure under the background error covariance constraints. Figure 12(a) shows a crude representation of the low latitude S − B temperature difference in Fig. 5. With a S − B surface pressure difference of 3 hPa (Fig. 7), the resulting solution density at 9.5 km is greater than the background by a bit more than 1%, roughly the required compensation amount (Fig. 12(b)).
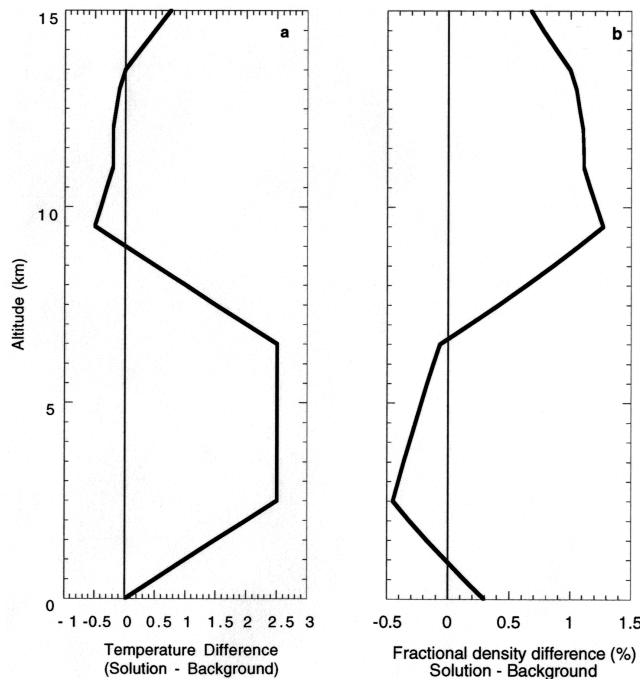
Features consistent with our hypothesis include 1) the sign change in the temperature bias near 300 hPa in Fig. 5, 2) the coincidence between the meridional extent of large temperature modifications in Fig. 5 and high humidities associated with the tropical Hadley circulation, 3) the coincidence of small S − B temperature differences south of 15S and the very dry subsidence zones in the subtropics and 4) the large, negative S − B specific humidity differences near 300 hPa at 5N and 20N in Fig. 8 which are likely due to the overestimated dry densities just below 9.5 km altitude as represented in Fig. 12(b). The large hydrostatic modification of densities peaked at 9.5 km in Fig. 12(b) also makes the solution's results at higher altitudes somewhat suspect.

6. Impact Summary

The impact of the observations on the solution is reflected in the mean and standard deviations of the solution minus background differences, the contribution to the penalty function and the improved error covariance of the solution. Because of the imperfect error covariances and lack of moisture above 300 hPa, some care must be taken in interpretation and drawing conclusions.

The improvement to the error covariance implicit in Eq. (3) reflects background and measurement error covariances and K, the gradient of the observations vector with respect to the model state. Improvement here is estimated as the square root of the variance of the solution divided by the variance of the background for the diagonal terms of the error covariance.

Temperature Improvement: The reduction of the background temperature error in Fig. 13 ranges from very little near the surface to a factor of $\sim$10 near 250 hPa. The largest improvement near 250 hPa where $\sigma_{\text{Tsol}}/\sigma_{\text{Tbac}}$ is 10–15% reflects the large error assigned to background temperature estimates at this altitude associated with the altitude of the tropopause at summer mid-latitudes. The temperature error improvements decrease below the 300 hPa level due to increasing water vapor at lower altitudes. Southern Hemisphere temperature improvements are also greater below 300 hPa reflecting the large moisture contrast associated with the winter-summer hemisphere asymmetry.
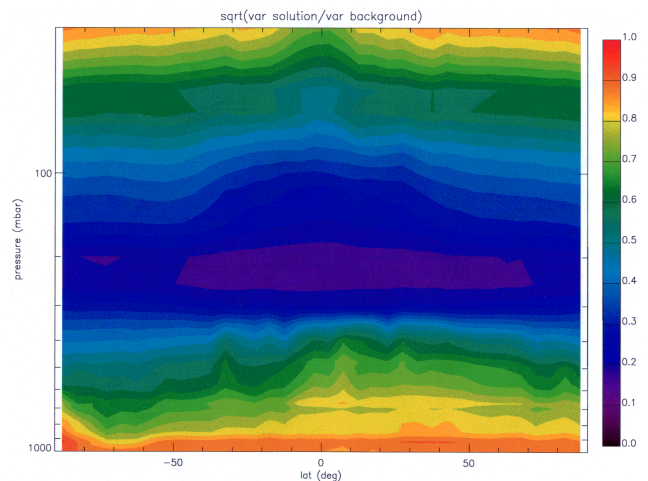

Fig. 12. Simple model of low latitude adjustment in the solution to compensate for lack of water above 300 mb. (a) Temperature difference (Solution − Background). (b) Fractional density difference (Solution − Background).

Fig. 13. Temperature error reduction ($\sigma_{\text{Tsolution}}/\sigma_{\text{Tbackground}}$).

Surface Pressure Improvement: The new pressure error estimate is 20 to 25% smaller than the background error estimate with relatively little dependence on latitude except close to the South Pole (Fig. 14). This cannot reflect the whole story because there should be a larger improvement in areas of sparse observations where the background surface pressure uncertainty must larger. Again the background error covariance needs to vary with location to reflect weaker knowledge in poorly observed areas.

Specific humidity Improvement: The specific humidity error in large regions of the troposphere was reduced to less than 60% of the background error (Fig. 15). The Q error reduction reaches a maximum in the mid-troposphere near the ITCZ where the solution error is less than 20% of the background error. The biggest disappointment is in the southern subtropics where the relatively small error reduction does not reflect the large mean adjustments in Fig. 8 and substantial discrepancies between the background and solution moisture estimates there in Fig. 9. The reason is the global error covariance in Fig. 4 does not reflect the systematic ECMWF

analysis errors in this region. There are signs that a weaker version of the same problem is occurring near 30N. Regarding the general impact on Southern Hemisphere moisture, Kursinski and Hajj (2000b) found the ECMWF analysis specific humidity errors in the Southern Hemisphere to be significantly larger than their Northern Hemisphere counterparts (Fig. 16). Their estimate of the reduction of the background moisture error (Fig. 17) is therefore somewhat larger than that in Fig. 15 in the Southern Hemisphere. Overall the GPS constraints should significantly improve the quality of global moisture analyses.

The magnitude of the penalty function provides some indication of the success of the 1DVar. The value of the penalty function achieved here, when normalized by the degrees of freedom (= the number of free parameter in the model), is roughly 4 times larger than optimal implying the solution reflects agreement between the background and observations more at the 2-sigma rather than 1-sigma level. Given the simplicity of the error covariances which contain no latitudinal dependence and the simple exponential decay refractivity
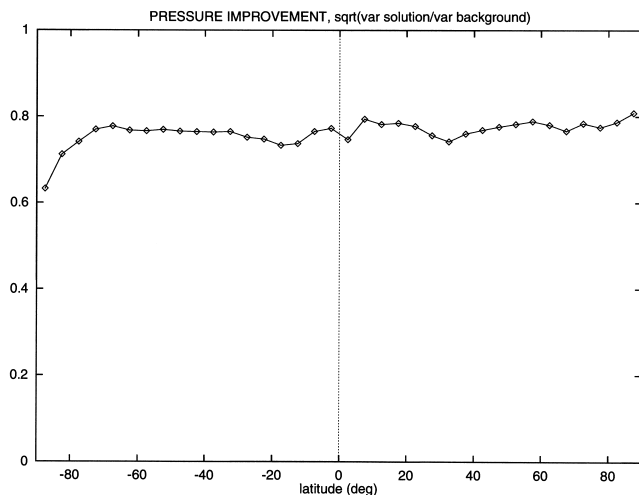

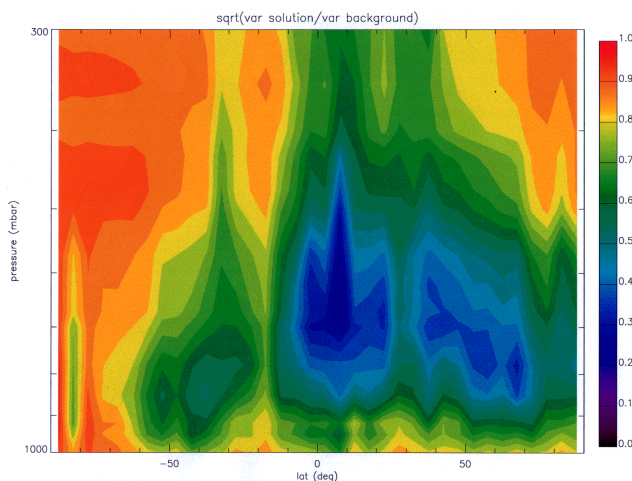Fig. 14. Surface pressure error reduction ($\sigma_{Psolution}/\sigma_{Pbackground}$).
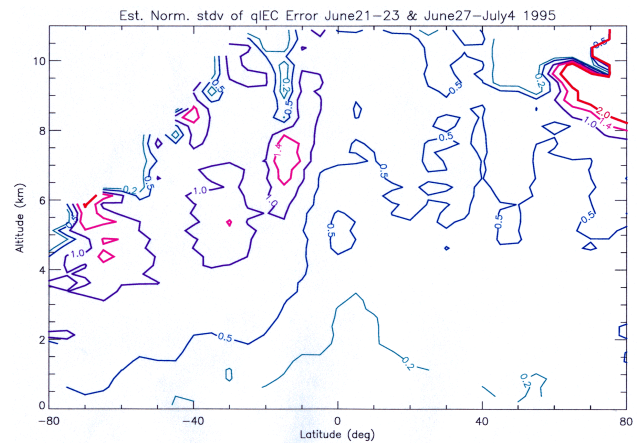

Fig. 16. Estimated fractional error in ECMWF global specific humidity analyses derived via comparison with GPS results (from Kursinski and Hajj, 2000b).
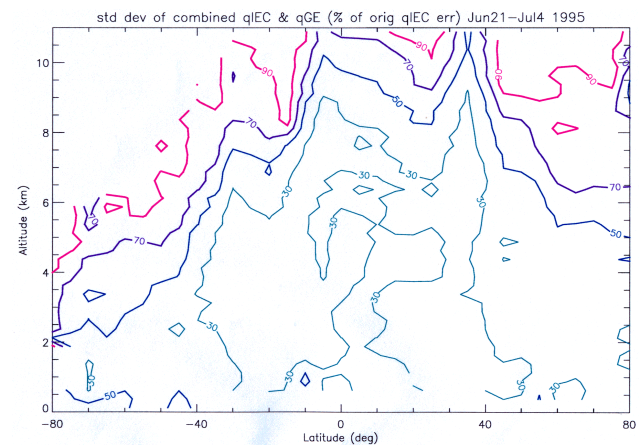

Fig. 15. Specific humidity error reduction ($\sigma_{Qsolution}/\sigma_{Qbackground}$).

Fig. 17. Expected reduction in ECMWF global specific humidity analysis errors ($\sigma_{w/GPS}/\sigma_{prior}$ (in %)) when GPS occultation data is assimiliated. Contours are in %. (from Kursinski and Hajj, 2000b).

covariance with diagonal terms taken from Kursinski *et al.* (1997), these initial results described here are encouraging.

References

Fjeldbo, G. F., V. R. Eshleman, and A. J. Kliore, The neutral atmosphere of Venus as studied with the Mariner V radio occultation experiments, *Astron. J.*, **76**, 123–140, 1971.

Gadd, A. J., B. R. Barwell, S. J. Cox, and R. J. Renshaw, Global processing of satellite sounding radiances in a numerical weather prediction system, *Q. J. Roy. Met. Soc.*, **121**, 615–630, 1995.

Healy, S. B. and J. R. Eyre, Retrieving temperature, water vapour and surface pressure information from refractive index profiles derived by radio occultation: a simulation study, *Q. J. Roy. Met. Soc.*, 2000 (in press).

Karayel, E. T. and D. P. Hinson, Sub-Fresnel-scale vertical resolution in atmospheric profiles from radio occultation, *Radio Sci.*, **32**(2), 411–423, 1997.

Kursinski, E. R., The GPS radio occultation concept: theoretical performance and initial results, Ph.D. thesis, Calif. Inst. of Technol., Pasadena, 1997.

Kursinski, E. R. and G. A. Hajj, A comparison of water vapor derived from GPS occultations and global weather analyses, *J. Geophys. Res.*, 2000a (in press).

Kursinski, E. R. and G. A. Hajj, Zonal variability and accuracy of water vapor estimated from GPS and global weather analyses, *J. Geophys. Res.*, 2000b (submitted).

Kursinski, E. R., G. A. Hajj, K. R. Hardy, L. J. Romans, and J. T. Schofield, Observing tropospheric water vapor by radio occultation using the Global Positioning System, *Geophys. Res. Lett.*, **22**, 2365–2368, 1995.

Kursinski, E. R., G. A. Hajj, W. I. Bertiger, S. S. Leroy, T. K. Meehan, L. J. Romans, J. T. Schofield, D. J. McCleese, W. G. Melbourne, C. L. Thornton, T. P. Yunck, J. R. Eyre, and R. N. Nagatani, Initial results of radio occultation observations of Earth's atmosphere using the Global Positioning System, *Science*, **271**, 1107–1110, 1996.

Kursinski, E. R., G. A. Hajj, K. R. Hardy, J. T. Schofield, and R. Linfield, Observing Earth's atmosphere with radio occultation measurements using GPS, *J. Geophys. Res.*, **102**(D19), 23429–23465, 1997.

Kursinski, E. R., G. A. Hajj, S. S. Leroy, and B. Herman, The GPS radio occultation technique, *Terrestrial, Atmopsheric and Oceanic Sciences (TAO)*, **11**, 53–114, 2000.

Leroy, S. S., Measurement of geopotential heights by GPS radio occultation, *J. Geophys. Res.*, **102**, 6971–6986, 1997.

Rocken, C., R. Anthes, M. Exner, D. Hunt, S. Sokolovskiy, R. Ware, M. Gorbunov, W. Schreiner, D. Feng, B. Herman, Y.-H. Kuo, and X. Zou, Analysis and validation of GPS/MET data in the neutral atmosphere, *J. Geophys. Res.*, **102**, 29849–29866, 1997.

Tsuda, T., M. Nishida, C. Rocken, and R. H. Ware, A Global Morphology of Gravity Wave Activity in the stratosphere revealed by the GPS occultation data (GPS/MET), *J. Geophys. Res.*, 1999 (submitted).

E. R. Kursinski (e-mail: erk@cobra.jpl.nasa.gov, kursinsk@atmo.arizona.edu), S. B. Healy, and L. J. Romans